Engineering 4 (2018) 822–830

Contents lists available at ScienceDirect

Engineering

journal homepage: www.elsevier.com/locate/eng

Research
Precision Engineering—Article

Engineered Functional Surfaces by Laser Microprocessing for Biomedical Applications

Guoqing Hu [a,b,#], Kai Guan [c,#], Libin Lu [a], Jiaru Zhang [a], Nie Lu [d], Yingchun Guan [a,b,e,*]

[a] School of Mechanical Engineering and Automation, Beihang University, Beijing 100083, China
[b] Hefei Innovation Research Institute, Beihang University, Hefei 230013, China
[c] Department of Oncology, Center of Excellence, BOE Hefei Digital Hospital Co., Ltd., Hefei 230013, China
[d] Beijing Long March Space Vehicle Research Institute, First Academy of the China Aerospace Corporation, Beijing 100076, China
[e] National Engineering Laboratory of Additive Manufacturing for Large Metallic Components, Beihang University, Beijing 100083, China

ARTICLE INFO

Article history:
Received 25 April 2018
Revised 12 June 2018
Accepted 18 September 2018
Available online 25 September 2018

Keywords:
Laser microprocessing
Functional surface
Metallic alloy
Niocompatibility
SERS

ABSTRACT

Metallic biomaterials are increasingly being used in various medical applications due to their high strength, fracture resistance, good electrical conductivity, and biocompatibility. However, their practical applications have been largely limited due to poor surface performance. Laser microprocessing is an advanced method of enhancing the surface-related properties of biomaterials. This work demonstrates the capability of laser microprocessing for biomedical metallic materials including magnesium and titanium alloys, with potential applications in cell adhesion and liquid biopsy. We investigate laser-material interaction, microstructural evolution, and surface performance, and analyze cell behavior and the surface-enhanced Raman scattering (SERS) effect. Furthermore, we explore a theoretical study on the laser microprocessing of metallic alloys that shows interesting results with potential applications. The results show that cells exhibit good adhesion behavior at the surface of the laser-treated surface, with a preferential direction based on the textured structure. A significant SERS enhancement of 6×10^3 can be obtained at the laser-textured surface during Raman measurement.

1. Introduction

Metallic biomaterials are used in various medical applications, mainly due to their attributes of high strength, fracture resistance, good electrical conductivity, and biocompatibility [1]. Surface modification of biomaterials is considered to be an effective method to control cell adhesion, migration, orientation, shape, and even gene expression in *in vitro* and *in vivo* studies [2–6]. For example, good adhesion between cells and implants is crucial for fracture repair, as it affects not only the growth and metabolism of bone tissue and physiology, but also the repair and reconstruction of bone tissue under conditions of injury [7–9]. Compared with conventional surface-modification techniques such as photolithography, electrospinning, electron beam lithography, and chemical patterning [10–12], the main advantages of laser techniques are the lack of contaminants, high enhancement factor, low cost with high uniformity and reproducibility, and capability to tailor topography at the microscale or even nanoscale. Therefore, laser microprocessing has attracted considerable attention from both scientists and engineers in recent years. Martínez-Calderon et al. [13] investigated the culturing capabilities of laser-induced periodic surface structures (LIPSS) on stainless steel, and found that cells preferentially align and attach to the LIPSS with particular direction. Cunha et al. [14] reported that the stretching of human mesenchymal stem cells (hMSCs) could be induced by LIPSS for orthopedic implants via ultrafast laser surface texturing. Dumas et al. [15] fabricated three types of biomimetic patterns on the surface of a titanium (Ti) alloy, thereby showing that the combination of LIPSS and micro pits could enhance osteogenic potential. As a promising biomaterial material with a degradation behavior and elastic modulus similar to human bones, magnesium (Mg) alloys have attracted a great deal of attention for use as implants [16–18]. However, high ion release and a tremendous change of local pH in the rapid degradation at the Mg alloy surface result in a survival environment that is quite severe for cells and that greatly reduces cell viability [12]. The improvement of commercial Mg alloys through corrosion resistance using laser surface

* Corresponding author.
E-mail address: guanyingchun@buaa.edu.cn (Y. Guan).
# These authors contributed equally to this work.

https://doi.org/10.1016/j.eng.2018.09.009

modification was subsequently proposed, and has been widely studied in the past decades [19,20]. To the best of our knowledge, cell behavior at the surfaces of laser-treated Mg alloys has not been reported in the public domain.

Moreover, liquid biopsies play an increasingly important role in the diagnosis and treatment of cancer due to their noninvasiveness, convenient sampling, and capability for real-time monitoring in the detection of cells and DNA [21–24]. Detection indicators with excellent specificity, sensitivity, and stability are very necessary in order to improve the accuracy and efficiency of lipid biopsies. Surface-enhanced Raman scattering (SERS) has been widely used for biomaterial analyses and the detection of low-concentration biochemical molecules based on vibrational spectroscopic information of molecules obtained by inelastic scattering with photons. In recent years, the periodic surface structures of detected substrates have been successfully employed to enhance Raman scattering, resulting in sensitive detection and efficient remediation. A variety of laser-induced SERS methods have been reported, most of which can be simply classified into two categories: silicon (Si) substrates and non-Si substrates. In regard to Si substrates, Xu et al. [25] found that micro- and nano-structures with particle sizes below 100 nm at the Si surface provided the greatest improvement in Raman scattering. Zhu et al. [26] reported that SERS enhancement factors as high as 3×10^7 had been achieved on laser-ablated gold (Au)-coated Si wafers with three-dimensional (3D) micro- or nano-structures for Rhodamine 6G (R6G) molecules, as a result of the enhanced surface area and Au nanoparticles with different sizes. Parmar et al. [27] fabricated nano-scaffolds decorated with metal nanoparticles on black Si substrates, showing that surface plasmonic effects and "hot spots" at laser-textured surfaces could lead to significant enhancement of the Raman signal. In regard to non-Si substrates, Buividas et al. [28] demonstrated a direct laser write approach to create nano-textured surfaces on sapphire; these surfaces showed a SERS signal up to 15 times higher with a signal uniformity two times better than commercial SERS-sensing substrates. Rebollar et al. [29] fabricated Au-coated LIPSS on spin-coated polymer thin films by means of a nanosecond laser, and investigated their characterization as substrates for SERS. The enhancement factor for the Au-coated substrates was estimated to be eight orders of magnitude, while an additional enhancement of around ten was mediated by the presence of LIPSS. Unfortunately, no reports on biocompatible substrates are available in the public domain.

The present work investigates the feasibility of laser microprocessing for biomedical metallic materials including Mg and Ti alloys, with potential applications in cell adhesion and liquid biopsy. Laser surface modification of a magnesium–gadolinium–gallium (Mg–Gd–Ga) alloy is examined first. Next, the biocompatibility—that is, cell viability and adhesion—of the as-received and laser-modified surfaces is evaluated using direct cell culture. We then examine the laser surface modification of a Mg-Gd-Ca alloy and apply the direct cell culture method to investigate initial cell viability and adhesion in order to compare the biocompatibility of the as-received and laser-modified surfaces. In addition, we investigate the capability of a femtosecond laser to achieve 3D LIPSS on a Ti alloy in order to enhance SERS measurement by enlarging the effective signal of the detected samples in order to simultaneously improve both efficiency and sensitivity.

2. Laser melting and nanostructuring of Mg alloys for biocompatibility enhancement

As a promising alternative to commercial Mg alloys, Mg–Gd-based alloys show a high performance in terms of biocompatibility and qualified mechanical properties. Like certain other rare earth elements, Gd has good biocompatibility. In addition, due to its large solubility in Mg at the eutectic temperature and intermetallic phase formation, introducing Gd into an alloy is beneficial in order to strengthen the formation of a solid solution and precipitation.

2.1. Experimental procedures

2.1.1. Materials

As a solid solution element in a Mg matrix and in the Mg-Gd eutectic phase of a Mg–6Gd-based alloy, calcium (Ca) is helpful to refine the grain and improve the yield strength of the alloy. Hence, hot-extruded Mg–6Gd–0.6Ca alloy bars were chosen in this case. The bar diameter was 9 mm, and a 4 mm slice was ground using silicon carbide (SiC) paper. After being washed with ethanol, the alloy was etched in a solution of 0.5% picric acid (1 g picric acid, 24 mL distilled water, 24 mL acetic acid, and 200 mL ethanol).

2.1.2. Laser processing

The Mg–6Gd–0.6Ca alloy surface was modified under argon (Ar) gas protection by a continuous-wave (CW) fiber laser centered at 1064 nm with a spot size of 100 μm. The scanning speed and the power density were respectively set at 70 $mm \cdot s^{-1}$ and 2.04×10^6 $W \cdot cm^{-2}$.

Surface texturing was carried out on the laser-melted surface using a Ti:sapphire chirped-pulse regenerative amplification laser system (with the center wavelength of 1064 nm, the pulse width of 800 fs, and the repetition rate of 400 kHz) at normal incidence in air at ambient temperature and pressure. The diameter of the Gaussian beam was measured to be about 35 μm. LIPSS were produced by adjusting the laser parameters.

2.1.3. Surface characterization

Surface topography was measured and characterized by optical spectroscope (LV150N, Nikon Corporation, Japan) and scanning electron microscope (SEM) with an energy dispersive spectrometer (SU8010, Hitachi Ltd., Japan). The phase was confirmed using an X-ray diffractometer (D/max2200PC, Rigaku Corporation, Japan).

2.1.4. Biocorrosion tests

The degradation rate of the Mg alloy was monitored by the evolved hydrogen volume. The hydrogen volume measurements of the as-received, laser-melted, and laser-melted-and-LIPSS specimens were studied in Hank's balanced salt solution (HBSS) for 34 h at 37 °C in a circulating water bath. The HBSS's volume per unit area of sample was 20 $mL \cdot cm^{-2}$. Fig. 1 shows the testing setup,

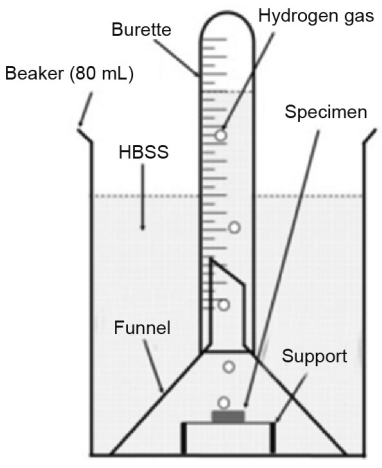

Fig. 1. Setup of hydrogen evolution measurement during immersion measurement.

and details of the measurement setup can be found in the literature [30]. The hydrogen evolution volume was measured every 2 h.

The electrochemical behavior was measured at 37 °C in HBSS using an electrochemical workstation (CHI660e, CH Instruments Inc., USA). The chemical composition of the HBSS solution is provided in Table 1. A three-electrode system was employed with a saturated calomel electrode as the reference electrode and a carbon electrode as the counter electrode; the specimen was the working electrode, with an exposed surface area of 0.64 cm^2. Tafel curves of the as-received and laser-modified specimens were measured at a scanning rate of 1 $mV \cdot s^{-1}$.

2.1.5. Cell culture

Murine calvarial preosteoblasts (MC3T3-E1, Peking Union Medical College, China) were applied to examine the *in vitro* biocompatibility of the Mg alloy. The MC3T3-E1 were cultured in 10% fetal bovine serum (FBS), Dulbecco's modified Eagle's medium (DMEM), 100 $\mu g \cdot mL^{-1}$ streptomycin at 37 °C, and 100 $U \cdot mL^{-1}$ penicillin in a humidified atmosphere of 5% carbon dioxide (CO_2).

2.1.6. Cell viability and cell morphology

The specimens were first sterilized by exposure to ultraviolet light radiation for 2 h. Cells were seeded by adding 70 mL of MC3T3-E1 cell suspension onto the surface, and were then cultured for 48 h. The initial density was 7×10^4 per specimen placed into a 24 well plate. For the cell morphology measurement, the cell-seeded scaffolds were cleaned three times with phosphate buffer solution (PBS) and fixed in paraformaldehyde for 30 min, while the specimens were rewashed three times using PBS and then dehydrated using graded ethanol. After vacuum drying and spraying with gold particles, the specimens were characterized using SEM. For the fluorescence microscopy investigation, the specimens were soaked in 70% ethanol solution for cell fixation, and cell components were colored using 5 $mg \cdot L^{-1}$ acridine orange dye. The fluorescence microscopy results were obtained by a fluorescence microscope (IX71, Olympus Corporation, Japan) equipped with a charge-coupled device (CCD) camera (iXON EM+ DU-897E-CSO-UVB, Andor Technology Ltd., Ireland).

Table 1
Chemical composition of HBSS.

Composition	Concentration ($mmol \cdot L^{-1}$)
Na^+	142.0
K^+	5.8
Mg^{2+}	0.8
Ca^{2+}	2.5
Cl^-	145.0
HCO_3^-	4.2
$H_2PO_4^-$	0.4
HPO_4^{2-}	0.3
SO_4^{2-}	0.8

2.2. Results and discussion

2.2.1. Morphology and microstructure

As shown in Fig. 2(a), the as-received Mg alloy consisted of an α-Mg matrix and β-phase Mg_5Gd [31,32]. After laser modification, the X-ray diffraction (XRD) results revealed that the laser-melted surface contained only the α-Mg phase; no Mg–Ca eutectic phase was found, either in the substrate or in the melted layer. This was attributed to the low Ca content in the Mg–6Gd–0.6Ca alloy [33]. Fig. 2(b) shows the typical solidification microstructure and surface morphology of the Mg–6Gd–0.6Ca after laser modification. A 400 μm thick melted layer with a solidification microstructure was generated, and the main content comprised small columnar grains of the α-Mg phase [34]. During laser surface processing, the temperature of the substrate increases dramatically when irradiated by the laser beam, and instantaneously reaches the melting point. When the laser beam moves on, the temperature drops immediately, leading to a huge temperature gradient and a rapid cooling rate in the melted layer. Consequently, no β-phase was found in the laser-melted layer. The surface topography of the LIPSS generated on the laser-melted surface is shown in Fig. 3(a). According to the surface profile illustrated in Fig. 3(b), the depth and period of the LIPSS are around 250 and 900 nm, respectively.

2.2.2. Hydrogen evolution

Fig. 4 presents the hydrogen evolution data for the as-received, laser-melted, and laser-melted-and-LIPSS samples during immersion in HBSS. The Mg corrosion reaction equation is provided below [35]:

$$Mg + 2H_2O \rightarrow Mg^{2+} + 2OH^- + H_2 \quad (1)$$

As shown in Eq. (1), Mg reacts with water (H_2O) to form hydrogen gas (H_2). The quantity of H_2 evolution is not influenced by the corrosion products formed at the surface of the Mg. The H_2 evolution rate, v_H ($mL \cdot cm^{-2} \cdot d^{-1}$), was estimated by measuring the total

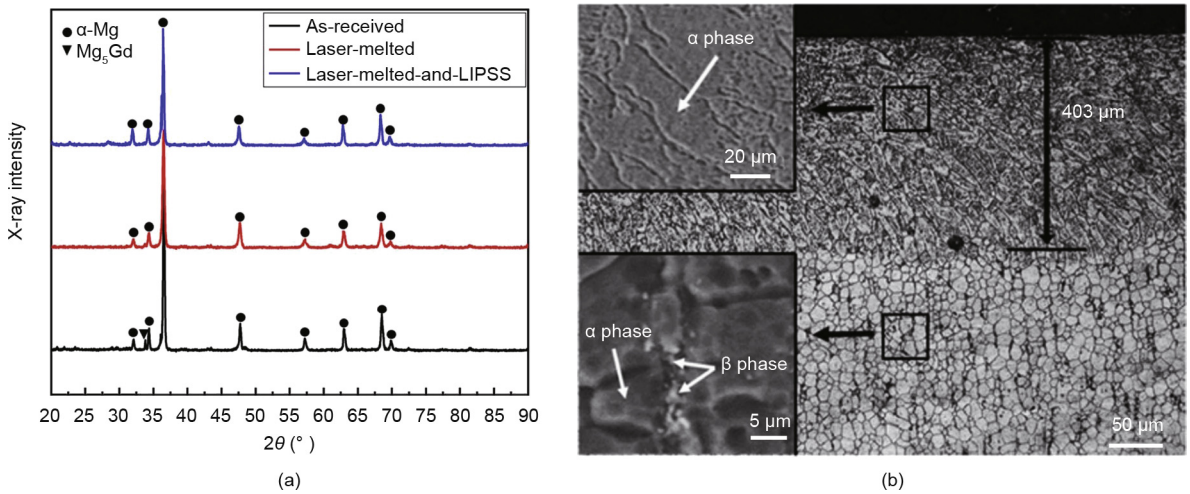

Fig. 2. Microstructure and phase compositions of Mg alloy before and after laser treatment. (a) XRD results; (b) cross-sectional view of laser-melted Mg alloy.

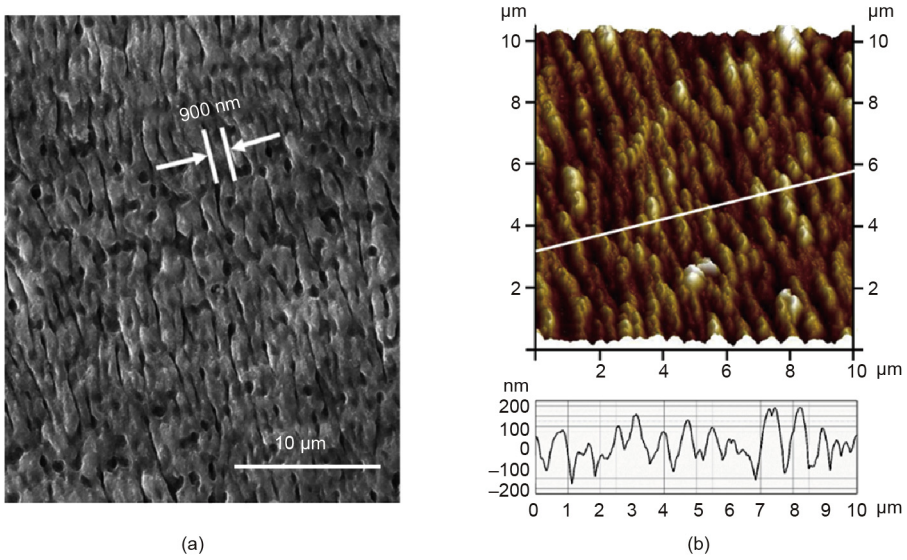

Fig. 3. (a) SEM and (b) atomic force microscopy (AFM) topography of LIPSS on the laser-melted Mg alloy surface.

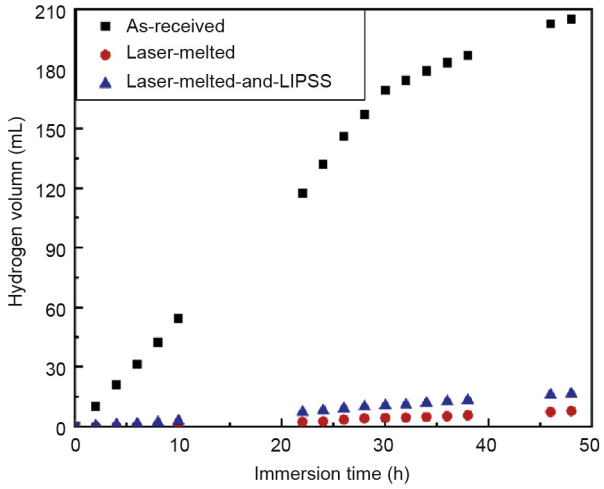

Fig. 4. Volume of hydrogen generated on as-received, laser-melted, and laser-melted-and-LIPSS surfaces during immersion in HBSS for 48 h.

H_2 released over a certain period of time [36]. Table 2 gives the total H_2 release and the H_2 evolution rate which corresponds to the average corrosion rate.

As shown in Fig. 4, the hydrogen volumes of the as-received, laser-melted, and melted-and-LIPSS specimens were 205, 7.8, and 16.6 mL, respectively, after 48 h immersion. This result indicates that both the laser-melted and the laser-melted-and-LIPSS specimens can effectively improve the corrosion resistance of the Mg–6Gd–0.6Ca alloy and significantly reduce the degradation rate in HBSS solution. The corrosion rate of the melted-and-LIPSS specimens, as estimated from the rate of H_2 evolution, was slightly higher than that of the melted specimens and was about 12 times slower than that of the as-received specimen. This may be due to the β-Mg_5Gd phase in the as-received specimen, which may act as a galvanic cathode and accelerate matrix corrosion [34]. After laser surface modification, the dissolution of the β phase into the matrix significantly reduced the amount of galvanic corrosion. Moreover, the LIPSS induced on the melted surface may increase the surface area and reduce the thickness of the melted layer, resulting in an increased corrosion rate compared with the laser-melted specimens. As shown in Table 2, the H_2 evolution rates of the as-received, melted, and melted-and-LIPSS specimens were 25.625, 0.975, and 2.075 $mL \cdot cm^{-2} \cdot d^{-1}$, respectively, after 48 h immersion. It is known that the H_2 adsorption rate tolerated by the human body is 2.25 $mL \cdot cm^{-2} \cdot d^{-1}$ [37]. Thus, the H_2 evolution rates of both the laser-melted and the laser-melted-and-LIPSS specimens were lower than the tolerance value of a human body.

Table 2
The total H_2 release and the H_2 evolution rate.

Specimens	Total H_2 release (mL)	H_2 evolution rate ($mL \cdot cm^{-2} \cdot d^{-1}$)
As-received	205.0	25.625
Laser-melted	7.8	0.975
Laser-melted-and-LIPSS	16.6	2.075

2.2.3. Electrochemical measurement

As shown in Fig. 5, a polarization study of the as-received, laser-melted, and laser-melted-and-LIPSS specimens was performed in HBSS. Table 3 summarizes their corrosion potential (E_{corr}) and

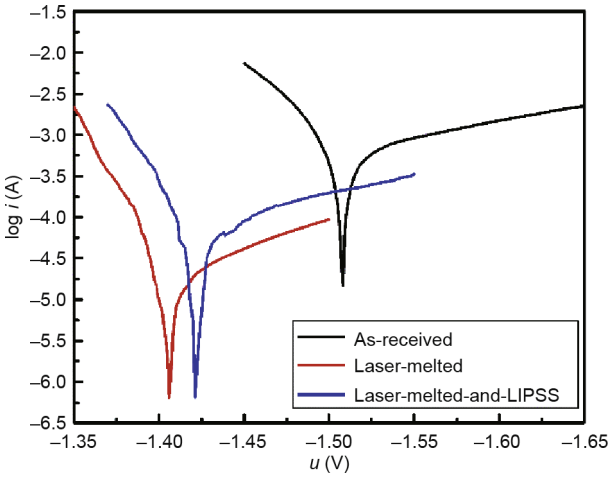

Fig. 5. Potentiodynamic polarization results of as-received, laser-melted, and laser-melted-and-LIPSS specimens in HBSS.

Table 3
E_{corr} and i_{corr} for as-received, laser-melted, and laser-melted-and-LIPSS in HBSS.

Specimens	E_{corr} (V)	i_{corr} (mA·cm^{-2})
As-received	−1.508	0.05540
Laser-melted	−1.406	0.00158
Laser-melted-and-LIPSS	−1.421	0.00484

corrosion current density (i_{corr}). The E_{corr} value of the laser-melted specimen exhibited a less-negative value (−1.406 V) than that of the as-received specimen (−1.508 V). After LIPSS were produced on the melted surface, the E_{corr} shifted slightly to a more negative value (−1.421 V), although this value was still less negative than that of the as-received microstructures. This finding indicates increased cathodic behavior compared with the melted microstructures, but decreased cathodic behavior compared with the as-received microstructures, mainly because the LIPSS induced on the melted surface may destroy the surface and reduce the thickness of the melted layer. This finding agrees well with the immersion test results shown in Fig. 4. Furthermore, the i_{corr} of the laser-melted-and-LIPSS specimen was much lower than that of the as-received specimen, but slightly higher than that of the laser-melted specimen. This indicates that the corrosion rate of the laser-melted-and-LIPSS specimen is lower than that of the as-received specimen but higher than that of the laser-melted specimen.

2.2.4. In vitro *biocompatibility*

As shown in Fig. 6, cell spreading behaviors including distribution and morphology were investigated at the surfaces of the as-received, laser-melted, and laser-melted-and-LIPSS specimens for 48 h after cell seeding. Due to poor corrosion resistance, no cell was observed on the as-received surface. After heavy corrosion took place during culturing, the formation of rod-like crystals was observed at the surface, as shown in Fig. 6(a). The viability of MC3T3-E1 cells is affected by the increased pH value and large release of Mg^{2+} ions caused by corrosion [38]. In contrast, cells exhibited good adhesion behavior and spread anisotropically on all laser-melted surfaces, as shown in Fig. 6(b) and 6(c). Fig. 6(c) indicates that the cell spreading was anisotropic on the laser-melted-and-LIPSS surfaces, with a large number of focal adhesions being presented as filopodia. Since filopodia usually act as nanosensors that allow cells to explore the external environment, the morphology of the filopodia indicates cell migration. High magnification of the focal adhesions in Fig. 6(d) reveals that the cell is migrating along the direction of the LIPSS, with a tree-like structure in the front and back areas.

Fluorescence investigation of the cell adhesions showed that cells at the laser-melted-and-LIPSS surfaces (Fig. 7(b)) presented an elongated shape with a smaller surface area than those at the laser-melted surfaces (Fig. 7(a)). This is mainly due to cell shape anisotropy during cytoskeleton reorganization caused by LIPSS, which can act as an anisotropic and persistent mechanical stimulus [17]. Cell density at the laser-melted surfaces was higher than at the laser-melted-and-LIPSS surfaces, due to the combined effect of corrosion resistance and surface topography. On the one hand, biocorrosion tests showed that the corrosion resistance of the laser-melted surface was better than that of the laser-melted-and-LIPSS surface, resulting in a lower pH value and Mg^{2+} concentration in the environment, which may better permit cells to survive and adhere. On the other hand, it has been reported that a surface structure with dimensions exceeding 70 nm may affect the integrin clustering efficiency, leading to a reduction of cell adhesion [20]. In this work, LIPSS with a period of 900 nm and depth of 250 nm were shown to reduce cell adhesion.

Therefore, we propose that the LIPSS at the melted surface is able to promote the growth of osteoblasts and accelerate ossification due to good adhesion; this can induce the cells that participate in fracture healing to gather at the end of a fracture and accelerate the healing of the fracture.

3. Large-scale nanostructuring of Ti alloys for SERS

Although substrates have recently been designed to allow sensitive detection in the form of a specific Raman fingerprint via

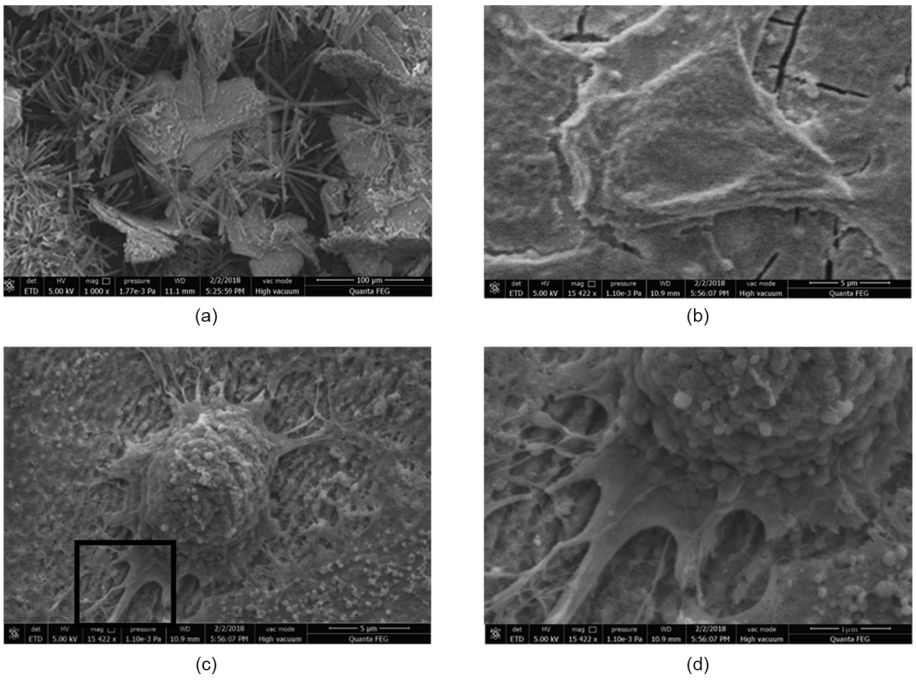

Fig. 6. SEM images of osteoblast shapes after cultured for 48 h on (a) as-received, (b) laser-melted, and (c) laser-melted-and-LIPSS surfaces; (d) zoomed-in area of cell protrusion, shown as the black box in (c).

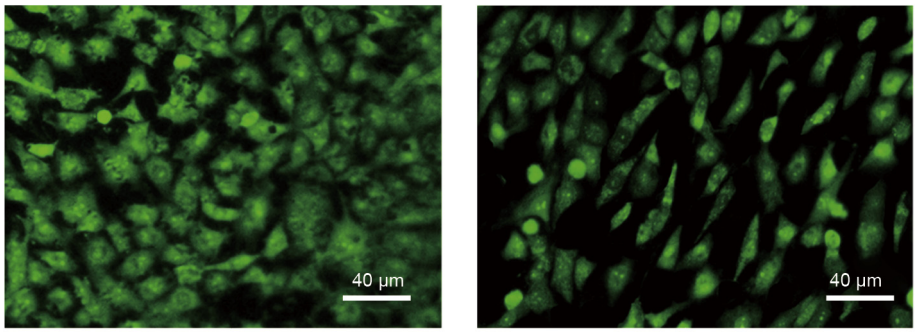

Fig. 7. Fluorescence images of osteoblast shapes on (a) laser-melted and (b) laser-melted-and-LIPSS surfaces after culturing for 48 h.

SERS, it is a challenging task to devise a simple approach for fabricating an SERS-responsive substrate based on biomedical materials and having biocompatibility. In this work, LIPSS were created on the surface of a bio-titanium alloy using laser irradiation with a femtosecond laser. To the best of our knowledge, this is the first report that realizes the capability of LIPSS to provide an enhanced spectroscopic signal via SERS, with the potential for application in the fields of bio-detection and bioimaging.

3.1. Experimental procedures

3.1.1. Materials

The Ti6Al4V substrate was cut into square samples with dimensions of 10 mm × 10 mm × 1 mm. Prior to laser processing, these samples were polished with SiC sandpaper in different grades of roughness (from 380 to 4000, in order to obtain a surface roughness less than 0.01 μm) and subsequently ultrasonically cleaned in acetone.

3.1.2. Laser processing

As shown in Fig. 8, LIPSS were fabricated by a Ti:sapphire laser system (with the center wavelength of 800 nm, the pulse width of 35 fs, and the repetition rate of 400 kHz) at normal incidence in air at ambient temperature and pressure. The diameter of the Gaussian beam was measured to be 35 μm. An electron beam evaporator was used to deposit gold (99.99% pure gold) thin film on the laser-fabricated Ti6Al4V surfaces for SERS.

3.1.3. Surface characterization

The surface topography was studied by SEM (SU8010, Hitachi Ltd., Japan) and atomic force microscopy (AFM; ICON, Bruker Corporation, USA) in contact mode. Nanoscope Analysis 1.4 software was applied to visualize and study the 3D AFM scans on 10 μm × 10 μm areas.

3.1.4. SERS measurement

Crystal violet (CV; ≥ 98% purity, Sigma-Aldrich) was applied as a probe molecule. A solution drop with a volume of about 5 μL was dropped onto the substrate and then dried in air. The dried substrate was used to carry out SERS signal measurement via Raman spectroscopy. The Raman microscope system (HORIBA Jobin Yvon, France) used to record the Raman spectra was equipped with a diode laser with a 532 nm excitation source and a CCD operating at a power level of around 5 mW. The acquisition time and accumulations were 10 s and 10, respectively. A 20× (numerical aperture = 0.45) microscope objective lens and a thermoelectrically cooled CCD array with a 600 $g \cdot mm^{-1}$ diffraction grating were used to detect the signals.

3.2. Results and discussion

3.2.1. Morphology evolution

When the incident laser fluence was close to the ablation threshold of titanium [39], 3D Au-coated LIPSS on a Ti6Al4V surface was fabricated. The 45° view of 3D LIPSS and the magnified view of the groove are respectively showed in Fig. 9(a) and 9(b). Periodic structure with periodicity of 600 nm on the groove and nanoparticles with diameters ranging from 60 to 200 nm randomly distributed on the above structure can be obviously observed. Besides, on a larger scale of 3D LIPSS, the average periodicity of 30 μm and the depth of 14 μm were measured using optical spectroscope as shown in Fig. 9(c). Furthermore, the cross-section profiles of the 3D LIPSS were also measured to confirm the results as shown in Fig. 9(d).

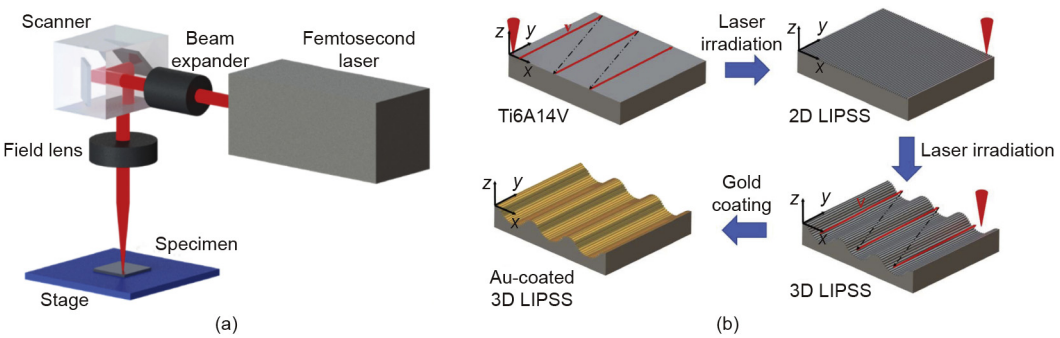

Fig. 8. (a) Experimental setup; (b) fabrication procedures of Au-coated 3D LIPSS.

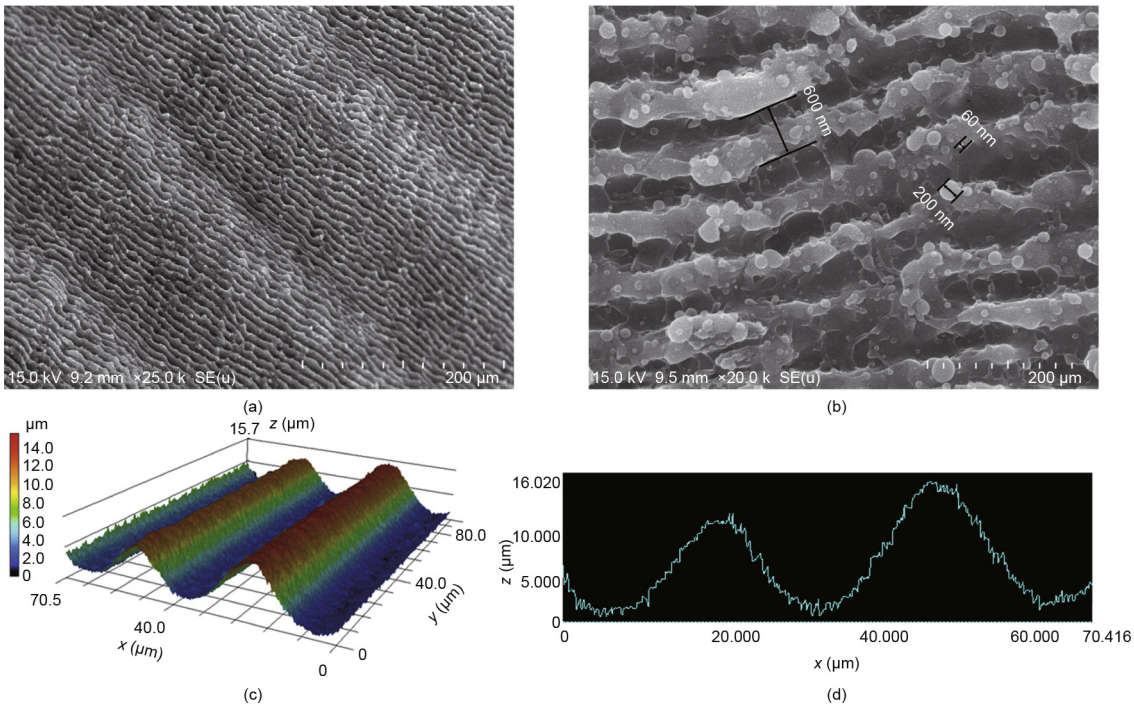

Fig. 9. Surface morphologies of 3D LIPSS fabricated on a Ti6Al4V surface. (a) SEM image; (b) magnified view of 3D LIPSS; (c) 3D optical image of the 3D LIPSS; (d) cross-section profiles of the 3D LIPSS.

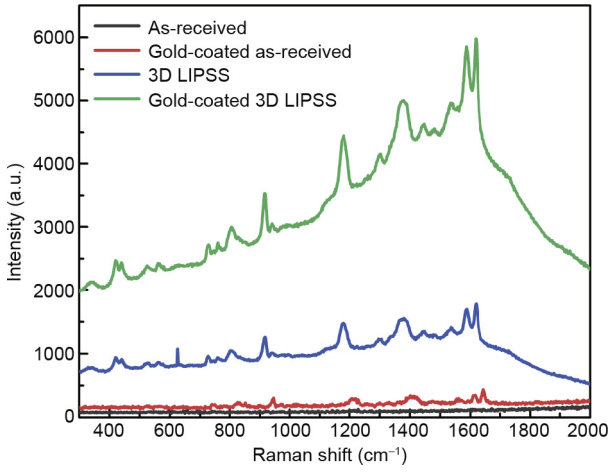

Fig. 10. The SERS spectra of 10^{-3} mol·L^{-1} CV molecules adsorbed on the as-received surface, Au-coated as-received surface, 3D LIPSS surface, and Au-coated 3D LIPSS surface.

3.2.2. SERS measurement

Fig. 10 shows the Raman spectrum of 10^{-3} mol·L^{-1} diluted CV on different dried substrates. The CV spectrum includes the characteristic bands that are attributed to the corresponding molecular vibrations [40,41]. For the as-received surface without coating, no Raman signal was observed. For the Au-coated as-received substrate, Raman signals with bands at 913, 1617, and 1646 cm^{-1} were obtained. This observation indicates that gold nanoparticles are efficient for SERS, which is in agreement with previous findings [42]. For the 3D LIPSS substrate, an intensity enhancement by a factor of 10^3 was observed, suggesting that 3D LIPSS are effective for the preparation of a SERS substrate. In regard to the Au-coated 3D LIPSS substrate, the sensitivity and intensity of the substrate were further enhanced after gold film deposition, since gold supports plasmons in the visible region [43]. Table 4 lists the corresponding Raman signal enhancement factors (EFs) of the 3D LIPSS and Au-coated 3D LIPSS for the bands at 913, 1176, 1374, and 1618 cm^{-1}. The EFs are the averaged values of five different locations. The results indicate that the highest EF reaches 6.7×10^3; this occurs at the Raman peak at 1374 cm^{-1} for the Au-coated 3D LIPSS.

Table 4
Enhancement factors for the 3D LIPSS SERS substrate.

Raman bands (cm^{-1})	Au-coated 3D LIPSS	3D LIPSS
913	2132	538
1176	2111	319
1374	6732	1074
1618	1123	279

Local surface plasmon resonance (LSPR) and surface plasmon polaritons (SPPs) will induce a significant enhancement of the local electromagnetic (EM) field, which is important for SERS [44,45]. As shown in Fig. 11, when the dimensions of a metal nanoparticle are less than the wavelength of the incident light, LSPR will occur, leading to collective oscillation of the valence electrons in the metal nanoparticle [46,47]. LSPR will concentrate the incident EM field around the nanoparticles. SPPs are the propagating charge oscillations excited by periodicity in a nanostructure. The SPPs will spread along a periodic nanostructure and generate a strong confinement of the EM field [48]. However, as SPPs propagate along the surface, they lose energy due to metal absorption, resulting in decay of the EM field [49]. Thus, the enhanced Raman signal is the result of LSPR caused by nanoparticles with diameters ranging from 60 to 200 nm generated on the 3D LIPSS, and by SPPs excited by the periodic LIPSS.

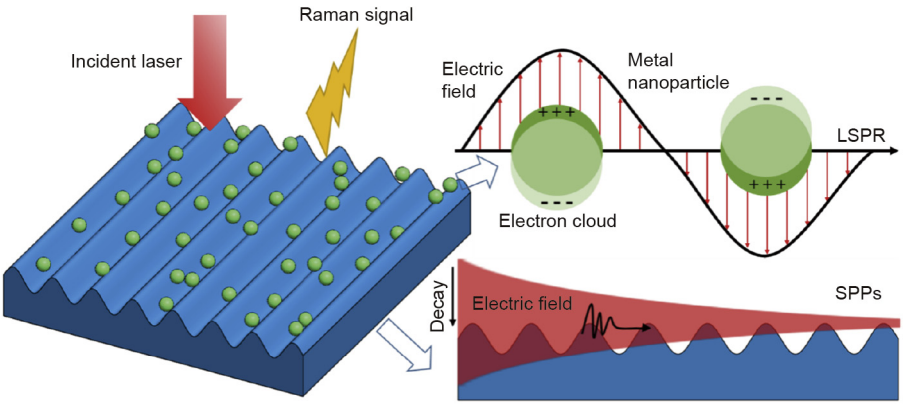

Fig. 11. Schematic of the SPPs and LSPR caused by laser irradiation during Raman measurement.

4. Conclusions

(1) The microstructure evolution, corrosion behavior, and biocompatibility of a Mg–6Gd–0.6Ca alloy before and after laser surface modification were carefully examined and compared. After laser surface modification, only α-Mg remained, and no precipitation of β-phase grains was found in the solidification microstructure. The thickness of the laser-modified layer was estimated to be 403 μm. Dissolution of the β-phase in the laser-melted region resulted in the significant reduction of galvanic couples. *In vitro* cell culture showed that MC3T3-E1 cells exhibited good adhesion behavior at the surface of all laser-treated specimens; in addition, cells at the laser-melted-and-LIPSS surfaces stretched heavily and presented long filopodia distributed at the outer edge.

(2) 3D LIPSS decorated with nanoparticles were prepared for SERS on a Ti6Al4V alloy substrate, fabricated by an ultrafast laser in a single step. 3D LIPSS provide high enhancement of SERS due to the increased surface area and nanoparticles. After coating with gold film, a significant enhancement of 6×10^3 was obtained in the Raman measurement. We suggest that the combined effect of LSPR by 3D LIPSS and nanoparticle "hot spots" is the main reason for the enhancement.

Acknowledgements

This work was supported by the National Key R&D Program of China (2018YFB1107400); the National Key Basic Research Program of China (2015CB059900); the National Natural Science Foundation of China (51705013); and the Beijing Natural Science Foundation (3162019 and J170002).

Compliance with ethics guidelines

Guoqing Hu, Kai Guan, Libin Lu, Jiaru Zhang, Nie Lu, and Yingchun Guan declare that they have no conflict of interest or financial conflicts to disclose.

References

[1] Pan F, Gao S, Chen C, Song C, Zeng F. Recent progress in resistive random access memories: materials, switching mechanisms, and performance. Mater Sci Eng Rep 2014;83:1–59.
[2] Xiong Y, Li H, Wang P, Liu P, Yan Y. Improved cell adhesion of poly(amino acid) surface by cyclic phosphonate modification for bone tissue engineering. J Appl Polym Sci 2018;135(21):46226.
[3] Escobar Ivirico JL, Bhattacharjee M, Kuyinu E, Nair LS, Laurencin CT. Regenerative engineering for knee osteoarthritis treatment: biomaterials and cell-based technologies. Engineering 2017;3(1):16–27.
[4] Guan Y, Zhou W, Zheng H. Effect of laser surface melting on corrosion behaviour of AZ91D Mg alloy in simulated-modified body fluid. J Appl Electrochem 2009;39(9):1457–64.
[5] Korhonen E, Riikonen J, Xu W, Lehto V, Kauppinen A. Cytotoxicity of mesoporous silicon microparticles with different surface modifications on ARPE-19 cells. Acta Ophthalmol 2014;92(S253):3257.
[6] Gupta AK, Gupta M. Synthesis and surface engineering of iron oxide nanoparticles for biomedical applications. Biomaterials 2005;26(18):3995–4021.
[7] Lo Celso C. Revealing the inner workings of human HSC adhesion. Blood 2017;129(8):921–2.
[8] Diener A, Nebe B, Lüthen F, Becker P, Beck U, Neumann HG, et al. Control of focal adhesion dynamics by material surface characteristics. Biomaterials 2005;26(4):383–92.
[9] Won JE, Yun YR, Jang JH, Yang SH, Kim JH, Chrzanowski W, et al. Multifunctional and stable bone mimic proteinaceous matrix for bone tissue engineering. Biomaterials 2015;56:46–57.
[10] Lee JY, Shah SS, Zimmer CC, Liu GY, Revzin A. Use of photolithography to encode cell adhesive domains into protein microarrays. Langmuir 2008;24(5):2232–9.
[11] Javaherian S, O'Donnell KA, McGuigan AP. A fast and accessible methodology for micro-patterning cells on standard culture substrates using Parafilm™ inserts. PLoS One 2011;6(6):e20909.
[12] Ross AM, Jiang Z, Bastmeyer M, Lahann J. Physical aspects of cell culture substrates: topography, roughness, and elasticity. Small 2012;8(3):336–55.
[13] Martínez-Calderon M, Manso-Silván M, Rodríguez A, Gómez-Aranzadi M, García-Ruiz JP, Olaizola SM, et al. Surface micro- and nano-texturing of stainless steel by femtosecond laser for the control of cell migration. Sci Rep 2016;6:36296.
[14] Cunha A, Zouani OF, Plawinski L, Botelho do Rego AM, Almeida A, Vilar R, et al. Human mesenchymal stem cell behavior on femtosecond laser-textured Ti-6Al-4V surfaces. Nanomedicine 2015;10(5):725–39.
[15] Dumas V, Guignandon A, Vico L, Mauclair C, Zapata X, Linossier MT, et al. Femtosecond laser nano/micro patterning of titanium influences mesenchymal stem cell adhesion and commitment. Biomed Mater 2015;10(5):055002.
[16] Manakari V, Parande G, Gupta M. Selective laser melting of magnesium and magnesium alloy powders: a review. Metals (Basel) 2017;7(1):2.
[17] Willbold E, Weizbauer A, Loos A, Seitz JM, Angrisani N, Windhagen H, et al. Magnesium alloys: a stony pathway from intensive research to clinical reality. Different test methods and approval-related considerations. J Biomed Mater Res A 2017;105(1):329–47.
[18] Guan YC, Zhou W, Li ZL, Zheng HY. Laser-induced microstructural development and phase evolution in magnesium alloy. J Alloys Compd 2014;582:491–5.
[19] Guan YC, Zhou W, Li ZL, Zheng HY. Influence of overlapping tracks on microstructure evolution and corrosion behavior in laser-melt magnesium alloy. Mater Design 2013;52:452–8.
[20] Coy AE, Viejo F, Garcia-Garcia FJ, Liu Z, Skeldon P, Thompson GE. Effect of excimer laser surface melting on the microstructure and corrosion performance of the die cast AZ91D magnesium alloy. Corros Sci 2010;52(2):387–97.
[21] Voelker R. Liquid biopsy receives approval. JAMA 2016;316(3):260.
[22] De Lázaro I, Kostarelos K. Optical diagnostics: nanosensors for liquid biopsies. Nat Biomed Eng 2017;1:0063.
[23] Diaz Jr LA, Bardelli A. Liquid biopsies: genotyping circulating tumor DNA. J Clin Oncol 2014;32(6):579–86.
[24] Schrump DS. Circulating tumor DNA: solid data from liquid biopsies. J Thorac Cardiovasc Surg 2017;154(3):1132–3.
[25] Xu K, Zhang C, Zhou R, Ji R, Hong M. Hybrid micro/nano-structure formation by angular laser texturing of Si surface for surface enhanced Raman scattering. Opt Express 2016;24(10):10352–8.

[26] Zhu Z, Yan Z, Zhan P, Wang Z. Large-area surface-enhanced Raman scattering-active substrates fabricated by femtosecond laser ablation. Sci China Phys Mech Astron 2013;56(9):1806–9.
[27] Parmar V, Kanaujia PK, Bommali RK, Vijaya Prakash G. Efficient surface enhanced Raman scattering substrates from femtosecond laser based fabrication. Opt Mater 2017;72:86–90.
[28] Buividas R, Stoddart PR, Juodkazis S. Laser fabricated ripple substrates for surface-enhanced Raman scattering. Ann Phys 2012;524(11):L5–L10.
[29] Rebollar E, Sanz M, Pérez S, Hernández M, Martín-Fabiani I, Rueda DR, et al. Gold coatings on polymer laser induced periodic surface structures: assessment as substrates for surface-enhanced Raman scattering. Phys Chem Chem Phys 2012;14(45):15699–705.
[30] Jang Y, Tan Z, Jurey C, Collins B, Badve A, Dong Z, et al. Systematic understanding of corrosion behavior of plasma electrolytic oxidation treated AZ31 magnesium alloy using a mouse model of subcutaneous implant. Mater Sci Eng C 2014;45:45–55.
[31] Ma C, Peng G, Nie L, Liu H, Guan Y. Laser surface modification of Mg–Gd–Ca alloy for corrosion resistance and biocompatibility enhancement. Appl Surf Sci 2018;445:211–6.
[32] Xiao B, Yang Q, Yang J, Wang W, Xie G, Ma Z. Enhanced mechanical properties of Mg–Gd–Y–Zr casting via friction stir processing. J Alloys Compd 2011;509(6):2879–84.
[33] Zhang X, Dai J, Yang H, Liu S, He X, Wang Z. Influence of Gd and Ca on microstructure, mechanical and corrosion properties of Mg–Gd–Zn(–Ca) alloys. Mater Technol 2017;32(7):399–408.
[34] Liu Y, Kang Z, Zhou L, Zhang J, Li Y. Mechanical properties and biocorrosion behaviour of deformed Mg–Gd–Nd–Zn–Zr alloy by equal channel angular pressing. Corros Eng Sci Technol 2016;51(4):256–62.
[35] Xin Y, Huo K, Tao H, Tang G, Chu P. Influence of aggressive ions on the degradation behavior of biomedical magnesium alloy in physiological environment. Acta Biomater 2008;4(6):2008–15.
[36] Taltavull C, Shi Z, Torres B, Rams J, Atrens A. Influence of the chloride ion concentration on the corrosion of high-purity Mg, ZE41 and AZ91 in buffered Hank's solution. J Mater Sci Mater Med 2014;25(2):329–45.
[37] Aghion EE, Arnon A, Atar D, Segal G, inventors; Biomagnesium Systems Ltd., assignee. Biodegradable magnesium alloys and uses thereof. WIPO Patent patent WO/2007/125532. 2007 Nov 8.
[38] Zheng Y, Gu X, Xi Y, Chai D. *In vitro* degradation and cytotoxicity of Mg/Ca composites produced by powder metallurgy. Acta Biomater 2010;6(5):1783–91.
[39] Mannion PT, Magee J, Coyne E, O'Connor GM, Glynn TJ. The effect of damage accumulation behaviour on ablation thresholds and damage morphology in ultrafast laser micro-machining of common metals in air. Appl Surf Sci 2004;233(1–4):275–87.
[40] Villa JEL, Santos DP, Poppi RJ. Fabrication of gold nanoparticle-coated paper and its use as a sensitive substrate for quantitative SERS analysis. Mikrochim Acta 2016;183(10):2745–52.
[41] Harraz FA, Ismail AA, Bouzid H, Al-Sayari SA, Al-Hajry A, Al-Assiri MS. Surface-enhanced Raman scattering (SERS)-active substrates from silver plated-porous silicon for detection of crystal violet. Appl Surf Sci 2015;331:241–7.
[42] Domingo C, Resta V, Sanchez-Cortes S, García-Ramos JV, Gonzalo J. Pulsed laser deposited Au nanoparticles as substrates for surface-enhanced vibrational spectroscopy. J Phys Chem C 2007;111(23):8149–52.
[43] Stiles PL, Dieringer JA, Shah NC, Van Duyne RP. Surface-enhanced Raman spectroscopy. Annu Rev Anal Chem 2008;1(1):601–26.
[44] Bauch M, Toma K, Toma M, Zhang Q, Dostalek J. Plasmon-enhanced fluorescence biosensors: a review. Plasmonics 2014;9(4):781–99.
[45] Caldarola M, Albella P, Cortés E, Rahmani M, Roschuk T, Grinblat G, et al. Non-plasmonic nanoantennas for surface enhanced spectroscopies with ultra-low heat conversion. Nat Commun 2015;6(1):7915.
[46] Kelly KL, Coronado E, Zhao L, Schatz GC. The optical properties of metal nanoparticles: the influence of size, shape, and dielectric environment. J Phys Chem B 2003;107(3):668–77.
[47] Li M, Cushing SK, Wu N. Plasmon-enhanced optical sensors: a review. Analyst 2015;140(2):386–406.
[48] Dong J, Zhang Z, Zheng H, Sun M. Recent progress on plasmon-enhanced fluorescence. Nanophotonics 2015;4(1):472–90.
[49] Homola J, Piliarik M. Surface plasmon resonance (SPR) sensors. Surface plasmon resonance based sensors. Springer, Berlin Heidelberg 2006;4:45–67.